JMEPEG (2012) 21:786–796
DOI: 10.1007/s11665-011-9876-5

1059-9495/$19.00

Two-Level Weld-Material Homogenization for Efficient Computational Analysis of Welded Structure Blast-Survivability

M. Grujicic, G. Arakere, A. Hariharan, and B. Pandurangan

(Submitted January 23, 2011)

The introduction of newer joining technologies like the so-called friction-stir welding (FSW) into automotive engineering entails the knowledge of the joint-material microstructure and properties. Since, the development of vehicles (including military vehicles capable of surviving blast and ballistic impacts) nowadays involves extensive use of the computational engineering analyses (CEA), robust high-fidelity material models are needed for the FSW joints. A two-level material-homogenization procedure is proposed and utilized in this study to help manage computational cost and computer storage requirements for such CEAs. The method utilizes experimental (microstructure, microhardness, tensile testing, and x-ray diffraction) data to construct: (a) the material model for each weld zone and (b) the material model for the entire weld. The procedure is validated by comparing its predictions with the predictions of more detailed but more costly computational analyses.

Keywords blast-survivability, computational engineering analysis, friction-stir welding, material-model development

1. Introduction

During the current decade, the U.S. military has placed increased emphasis on the development of improved light-weight body-armor and lightweight vehicle-armor systems as well as on the development of new high-performance armor materials/structures (to properly respond to the new enemy threats and warfare tactics). As a result, the U.S. ground forces are being continuously transformed to become faster, more agile, and more mobile so that they can be quickly transported to warfare/peace-keeping operations conducted throughout the world. As part of this effort, a number of research and development programs are under way with the main goal to engineer light-weight, highly mobile, transportable, and lethal battlefield vehicles with weight under 20 tons. To attain this goal, significant advances are needed in the areas of light-weight structural- and armor-materials development (including light-weight metallic materials such as aluminum- and titanium-based structural and armor-grade alloys). Due to complex geometry/topology of the military battle-field and tactical vehicles' (metallic-armor) body structures, these structures are typically fabricated by welding separately manufactured aluminum- and titanium-alloy components. Unfortunately, the high-performance aluminum- and titanium-alloy grades used in vehicle-armor applications are normally not very amenable to conventional fusion-based welding technologies, mainly due to the fact that the resulting weld-zone and/or heat-affected zone mechanical (and often corrosion) properties are quite deficient in comparison to their base-metal counterparts (Ref 1-4). In addition, the conventional welding processes are often not very economical or environment friendly. Most of the aforementioned shortcomings of the conventional welding processes when used in armor-grade aluminum/titanium-alloy-joining applications are remedied by the use of the so-called Friction Stir Welding (FSW) solid-state process.

FSW was invented and patented by The Welding Institute (UK) in the early 1990s (Ref 5). The basic principle of FSW is demonstrated in Fig. 1 using the example of flat-butt welding. The two plates (the workpiece) to be joined are rigidly clamped and placed on a backing plate. A rotating tool, consisting of a profiled pin and a shoulder, is forced down into the workpiece until the shoulder meets the surface of the workpiece. The workpiece material adjacent to the tool is thereby frictionally heated to temperatures at which it is softened/plasticized. As the tool advances along the butting surfaces, thermally softened workpiece material in front of the tool is back-extruded around the tool, stirred/heavily deformed (this process also generates heat), and ultimately compacted/forged into the tool-wake region to form a joint/weld.

When analyzing the weld formation during FSW, a distinction is made between the so-called advancing side of the weld (the side where the tangential component of the tool rotational speed is in the same direction as the tool travel direction) and the "retreating side" (the side where the tangential component of the tool rotational speed is opposite to the tool travel direction). Due to the differences in mass and heat transport and material deformation history, an FSW joint is typically asymmetric relative to the plane of the butting surfaces (Ref 1-3, 6, 7).

M. Grujicic, G. Arakere, A. Hariharan, and **B. Pandurangan**, Department of Mechanical Engineering, Clemson University, 241 Engineering Innovation Building, Clemson, SC 29634-0921. Contact e-mail: gmica@clemson.edu.

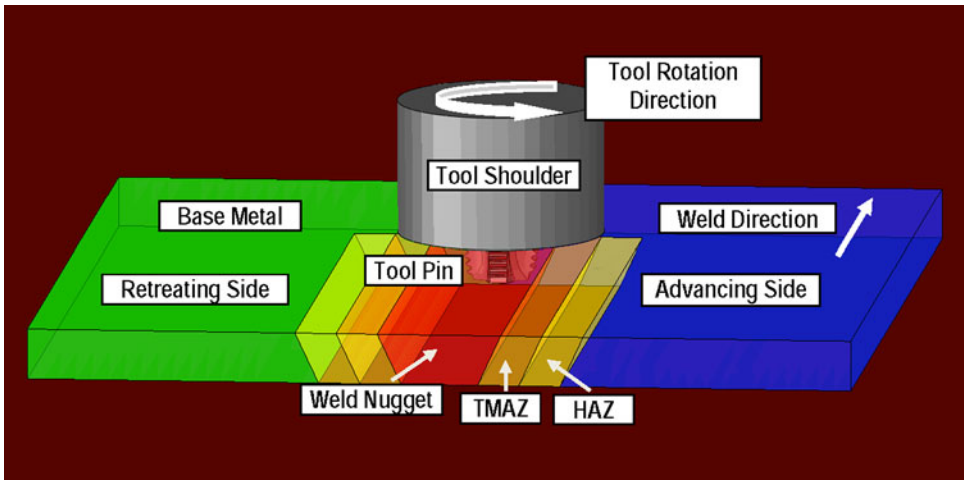

Fig. 1 A schematic of the friction stir welding (FSW) process used to fabricate a flat-butt joint. Four typical microstructural zones associated with the FSW process are also labeled

Macrographical and micrographical examinations of a typical friction-stir welded flat-butt joint reveal the presence of four distinct microstructural zones (Ref 7):

(a) a base-metal or un-affected zone which is far enough from the weld so that material microstructure/properties are not altered by the joining process;
(b) the heat-affected zone (HAZ) in which material microstructure/properties are affected only by the heat generated during the FSW process. While this zone is normally found in the case of fusion-welds, the nature of the microstructural changes may be different in the FSW case due to generally lower temperatures and a more diffuse heat source. Typical microstructural changes which influence the HAZ mechanical properties include the dissolution and coarsening of precipitates (in the case of heat-treatable aluminum-/titanium-alloy grades) and recovery-based dislocation density reduction (in the case of cold-worked heat-treatable and non-heat-treatable alloy grades);
(c) the thermo-mechanically affected zone (TMAZ) which is located closer than the HAZ zone to the butting surfaces. Consequently, both the thermal and the mechanical aspects of the FSW process affect the material microstructure/properties in this zone. Typically, the original grains are retained in this zone although they may have undergone severe plastic deformation. The dislocation density is generally increased relative to its base-metal level while the precipitates are greatly affected by the coarsening and dissolution processes; and
(d) the weld *nugget* is the innermost zone of an FSW joint. As a result of the way the material is transported from the regions ahead of the tool to the wake regions behind the tool, this zone typically contains the so called onion-ring features. The material in this region has been subjected to most severe conditions of plastic deformation and high-temperature exposure and consequently contains a very-fine dynamically recrystallized equiaxed grain microstructure. The presence of this fine-grain microstructure often has a beneficial effect in promoting fine scale re-precipitation in the case of heat-treatable alloy grades. The four aforementioned zones are sketched and labeled in Fig. 1.

Over the last 10 to 15 years, it has been clearly established that FSW provides a number of advantages when used for joining low melting point alloys (in particular, aluminum alloys, the alloys which have a great industrial importance). Among these advantages are the fact that, except for the highest-strength aluminum alloy grades, relatively inexpensive tool-steel based FSW tools could be utilized and high production rates realized while producing welds with good mechanical/structural integrity and visual appearance. Additional main advantages of the FSW process can be summarized as follows: (a) the process can be used for all welding positions (e.g., horizontal, vertical, overhead, orbital, etc.) and can, in each case, be fully automated to ensure high productivity and repeatable quality; (b) weld thicknesses in a range between ca. 0.5 and 65 mm can be produced in a single pass; (c) dissimilar alloy grades which are not amenable to fusion welding can be FSWed; (d) the extent of associated thermal distortion and microstructural/property changes is greatly reduced; (e) lower weld-surface preparation requirements (no oxide layer removal necessary); (f) consumables, filler materials or shielding gases are not used; (g) no harmful environmental effects/agents present such as UV radiation, spatter, weld fume, high electric current, and electromagnetic fields; (h) the process is highly energy efficient; (g) limited maintenance and spare part inventory for the FSW equipment is required; (i) due to the flat nature of the weld surfaces, less post weld machining is required.

The main limitations/shortcomings of the FSW process are generally identified as: (a) large clamping and shoulder-workpiece contact forces accompany the process which requires the use of high-stiffness clamping and FSW welding equipment; (b) at the completion of the FSW process, an exit hole is left in the weldment; (c) high level of geometrical conformability between the workpiece components is critical; (d) high capital equipment, operational, and licensing costs; and (e) if process parameters are not properly adjusted, defective joints may result.

The main FSW process parameters which control weld quality, process efficiency, and tool longevity are: (a) tool-travel/welding speed; (b) tool rotation speed; (c) tool geometry, cooling tilt angle, and plunge depth (in the case of displacement control) or plunge force (in the case of force control).

Additional parameters that influence the FSW process and the weldment are weld gap, workpiece thickness variation/mismatch, and clamping/welding machine stiffness. However, these parameters cannot be readily controlled (Ref 8).

Currently, FSW is being widely used in many industrial sectors such as shipbuilding and marine, aerospace, railway, land transportation, etc. This joining technology is, in principle, suitable for the fabrication of the welds of different topologies such as: 90° corner, flat-butt, lap, T, spot, fillet and hem joints, as well as to weld hollow objects, such as tanks and tubes/pipes, stock with different thicknesses, tapered sections, and parts with three-dimensional contours (Ref 9).

While in principle, many problems associated with fusion welding of the advanced high-strength aluminum and titanium alloys used in military-vehicle applications can be overcome through the use of FSW, the introduction of this joining process into the fabrication of advanced military-vehicle structures is not straight forward and entails a comprehensive multi-step approach. One such approach, based on the concurrent and interactive considerations of the key aspects associated with the components/vehicle design/manufacturing and testing, was recently proposed by the authors (Ref 9). One of the steps in this approach involves the use of computer-aided non-linear dynamics engineering analyses to predict (computationally) blast-survivability of the military-vehicle (look-alike) test-structures. As pointed out earlier, such structures are constructed by welding separately manufactured metallic components. In order for the aforementioned computational analysis of test-structure survivability to be reliable, it is critical that all the welds (and all the zones within the welds) be represented explicitly. Due to a relatively small length-scale of the FSW weld zones, this requirement typically results in finite-element models containing a large number (often in the range of several millions) of elements. The resulting large number of degrees of freedom and the associated very small computational time increments place a formidable demand on to the computational memory/storage requirements and lead to often unexpectedly long wall clock simulation times. In this study, a new two-level homogenization procedure is proposed and implemented to reduce the memory/storage requirements and increase the computational speed. Within the first level of homogenization, homogenized effective properties are determined for each FSW zone. Within the second level of homogenization, homogenized properties of the entire FSW-joint local cross section are computed. The procedure is validated against the results of the computational analyses in which weld zones are accounted for explicitly and against the available experimental results.

The organization of the article is as follows: A brief overview of the experimental techniques employed in this study, and the results obtained is presented in section 2. Parameterization of the base-metal and the weld-nugget materials within an FSW joint is presented in section 3. The two-level material-homogenization procedure is introduced and discussed in section 4. Validation and verification of this procedure is presented in section 5. A brief summary of the main findings obtained in the present work is presented in section 6.

2. Experimental Procedures and Results

All the experimental and the computational work carried out in this article involved AA2139 (an age-hardenable quaternary Al-Cu-Mg-Ag) alloy in a T8 (quenched + cold-worked + artificially aged) temper condition. The experimental work involved: (a) flat-butt FSW joining of 25.4 mm thick AA2139 plates; (b) quasi-static tensile testing of the base-metal and weld-nugget material properties in the weld direction; (c) quasi-static transverse (across-the-weld) tensile properties of the weldment; (d) measurements of microhardness distribution over the transverse cross section of the weld; and (e) x-ray-diffraction-based determination of the residual stresses within the weld and the surrounding base-metal. A brief description of each of the above-mentioned experimental procedures is provided below.

2.1 Flat-Butt Friction-Stir Welding

Flat-butt friction-stir welding of AA2139-T8 plates was performed at the Edison Welding Institute (Ref 10). The welding was performed under the following process parameters: (a) a two piece (flat-bottom shoulder + conical pin) four-flat left-handed thread FSW tool made of 350 M tool-steel; (b) tool travel and rotational speeds of 50 mm/min and 150 rpm, respectively; and (c) tool vertical and traverse loads of 55,600 and 26,600 N, respectively. A top-view of a typical AA2139-T8 flat-butt weld is shown in Fig. 2(a). The corresponding macrograph of the weld transverse cut section, clearly revealing the three weld zones, is depicted in Fig. 2(b).

2.2 Quasi-Static Longitudinal Tensile Testing

Room-temperature quasi-static (average engineering-strain rate $\sim$ 8e−4 s^{-1}) tensile mechanical properties of AA2139-T8 base-metal and weld nugget are determined using sub-size round bar specimens with a 25.4 mm gauge-length and 6.35 mm gauge-diameter. In the base-metal case both the

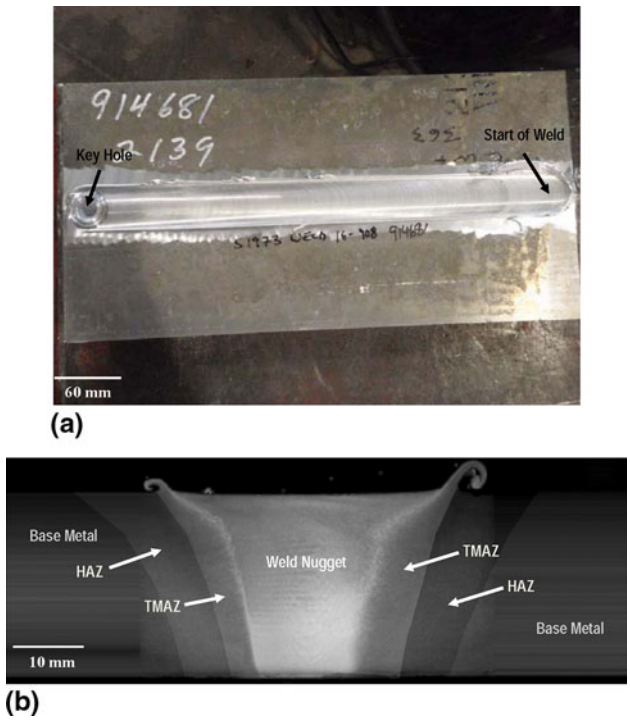

Fig. 2 (a) Top view and (b) transverse section macrograph of a AA2139-T8 flat-butt joint

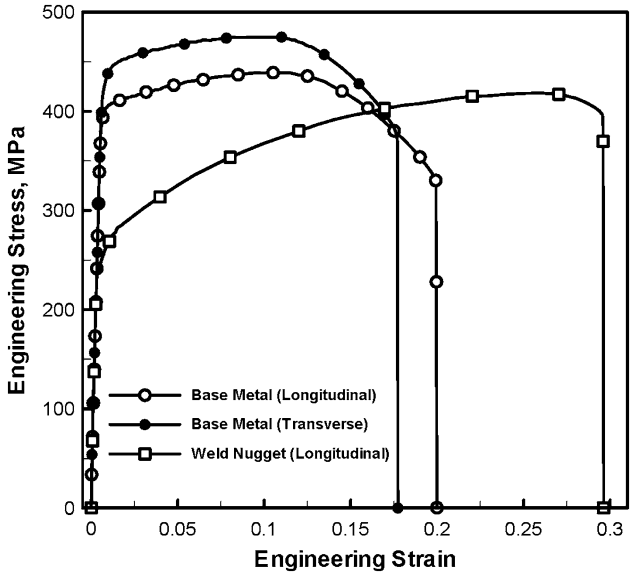

Fig. 3 Longitudinal and transverse base-metal and longitudinal flat-butt FSW weld-nugget engineering-stress vs. engineering-strain tensile-test curves in AA2139-T8

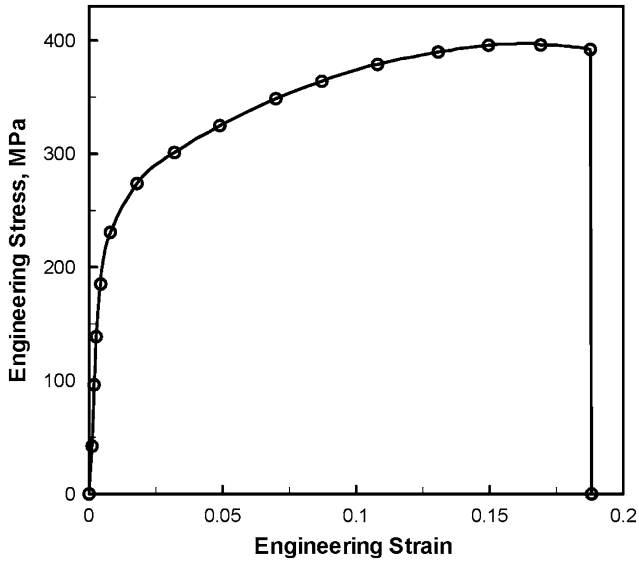

Fig. 4 Engineering-stress vs. engineering-strain transverse tensile-test curves in a FSW flat-butt AA2139-T8 weld

longitudinal (along the weld direction) and the transverse specimens were tested, while in the weld-nugget case, due to limited extent of the weld in the transverse direction, only the longitudinal samples (with their centerline located on the weld mid-thickness plane) were used. The resulting longitudinal/transverse base-metal and longitudinal weld-nugget engineering-stress versus engineering-strain data (averaged over three specimens, in each case) are displayed in Fig. 3. In all the cases, necking and ultimate fracture occurred within the specimen gauge-length and the fracture surface had a dimpled appearance, a defining characteristic of void-nucleation, growth, and coalescence-based ductile failure.

2.3 Quasi-Static Transverse Tensile Testing

Room-temperature quasi-static (average engineering-strain rate $\sim$4e−4 s^{-1}) transverse tensile mechanical properties of AA2139-T8 weldment are determined using square bar specimens with a 50.8 mm gauge-length and 25.4 mm square cross section edge-length (to enable monitoring of strain localization during the tensile test). The gauge-length was divided (using fiduciary marks) into eight 6.35 mm long segments to monitor the progress of strain localization. The resulting transverse tensile engineering-stress versus engineering-strain data (averaged over three specimens, in each case) are displayed in Fig. 4. In all the cases, necking and ultimate fracture occurred within the HAZ and the fracture surface had a dimpled appearance as in the case of the base-metal/weld-nugget materials.

2.4 Microhardness Measurements

Vicker's-type microhardness testing was undertaken using a Buehler 1600-6100 microhardness tester, at a load of 2 N and an application time of 10 to 15 s, in accordance with ASTM E3841. Microhardness measurements were conducted over the entire weld transverse cross-sectional area. The individual measurements were located at the nodes of a square-grid with the square edge-length of 0.5 mm.

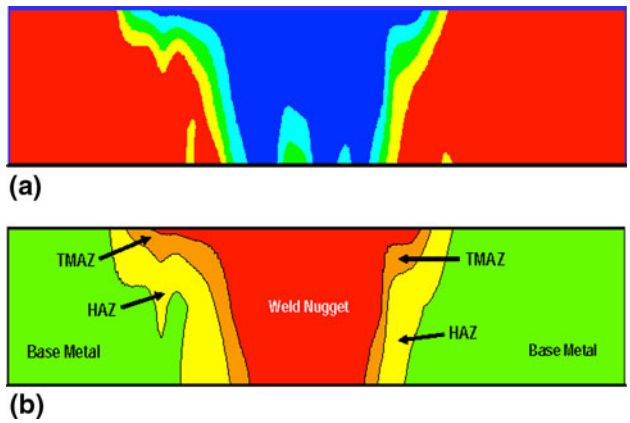

Fig. 5 (a) An example of a typical Vickers microhardness field plot over a transverse section of a AA2139-T8 FSW flat-butt joint; and (b) the associated partitioning of the FSW joint into separate weld zones

The Vickers microhardness number (in kgf/mm^2) is calculated using the following relation: $HV_{0.200} = 1.854\ F/d^2$ where the loading force F (=0.2 kgf) and d (in mm) is the diagonal mean value of the projected indentation. An example of the results obtained in the form of a microhardness contour plot, is displayed in Fig. 5(a). Based on the results displayed in this figure and the FSW macrograph displayed in Fig. 2(b), a schematic of the FSW flat-butt joint is provided in Fig. 5(b) in which different microstructural/properties zones are delineated.

2.5 X-ray Diffraction Residual-Stress Measurements

FSW-induced residual stresses in AA2139-T8 weldments are measured by carrying out standard x-ray diffraction experiments on a Scintag Polycrystalline-Texture-Stress (PTS) four-axis goniometer for stress and texture analysis with unrestricted 2θ range (from −2° to +162°) at an operating voltage of 18 kV. The corresponding Cu_α x-ray wave length is 0.031 nm. The reflections from the {311} family of planes,

representing the local poly-crystalline material state, are used in the residual-stress measurements since these planes are known to be less sensitive to inter-granular strain development (Ref 11, 12). The measurements were carried out over the top and the bottom portion of the flat-butt welded plates and it is assumed that the residual stresses in the portion of the weldment sandwiched by these two surfaces can be obtained using a simple linear interpolation procedure. It should be recognized, however, that the x-ray diffraction technique employed mainly characterizes the in-plane stress state in a region adjacent to the test-sample surface and that the through-the thickness residual stresses are not quantified. To quantify the in-plane residual stresses, the so-called $\sin^2\psi$ technique was employed (Ref 13), where ψ is the angle between the surface normal and the normal to the diffracting ({311}) crystallographic planes. The basic premise of this technique is that due to the presence of in-plane stress/strains, the spacing of the diffracting crystallographic planes changes continuously with the inclination angle ψ. To quantify the effect of in-plane directions on the accompanying normal stress/strain, a reference direction is selected in the test sample surface and the azimuthal angle ϕ used to specify the orientation of these directions. In the case of shear-free bi-axial (in-plane) stress field in an un-textured material, the normal engineering strain associated with an azimuthal angle ϕ and an inclination angle ψ, can be defined as:

$$\varepsilon_{\phi\psi} = \frac{d_{\phi\psi} - d}{d_0} = \frac{s_2}{2}\sigma_\phi \sin^2\psi + s_1(\sigma_{11} + \sigma_{22}) \qquad \text{(Eq 1)}$$

where $s_1 = \frac{-\nu}{E}$, $s_2 = \frac{(1+\nu)}{E}$, E is the Young's modulus, ν the Poisson's ratio, σ_ϕ the normal stress in the azimuthal ϕ-direction and σ_{11} and σ_{22} the associated principal stresses.

According to Eq 1, σ_ϕ can be computed from the slope of the $\varepsilon_{\phi\psi}$ versus $\sin^2\psi$ plot. When this procedure is repeated for two or more azimuthal ϕ directions, the in-plane residual-stress state, as defined by its principal stress components σ_{11} and σ_{22}, can be determined. In the aforementioned procedure, it was assumed that the unstressed inter-planar spacing d_0 is known. As shown by Peel et al. (Ref 14), d_0 can also be determined from the foregoing x-ray diffraction analysis provided the measurements are carried out along two mutually orthogonal azimuthal directions.

The procedure described above was used to quantify both the longitudinal and the transverse residual stresses on the top and the bottom test-sample surfaces along a line running orthogonal to the weld direction. An example of the typical results obtained in this portion of the study is displayed in Fig. 6(a) and (b).

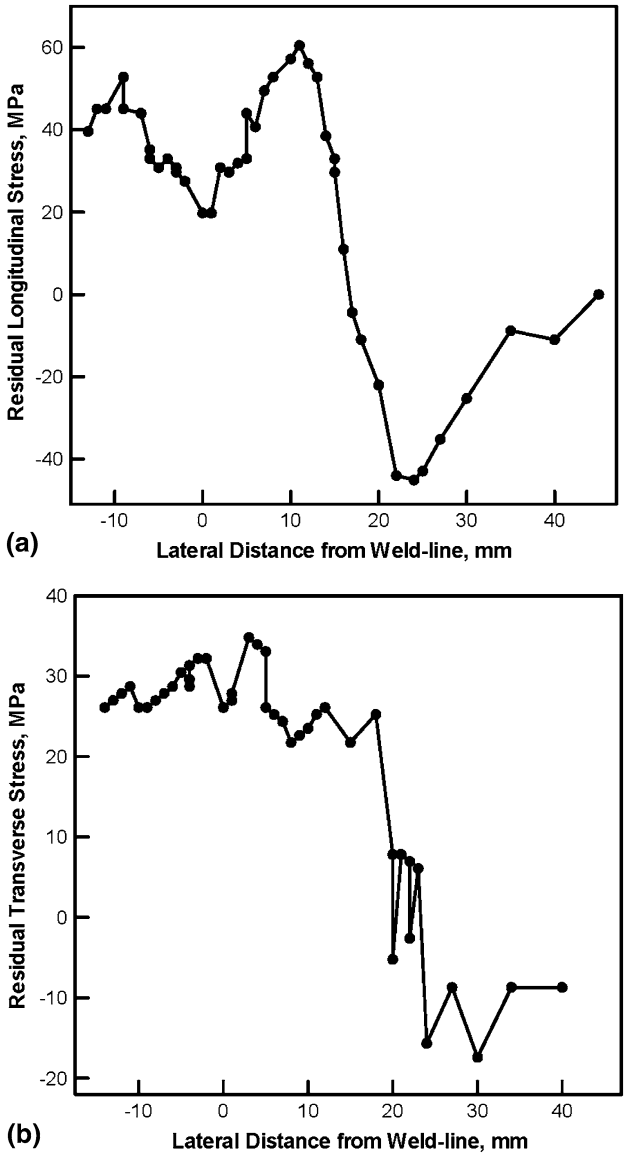

Fig. 6 Variation of the (a) longitudinal and (b) transverse residual stresses as a function of the distance from the weld-line. Data pertaining to the advancing side of the weld joint are on the right-hand side of the plot

3. Base-Metal and Weld-Nugget Material-Models Parameterization

In this section, the (averaged) longitudinal/transverse base-metal and weld-nugget engineering-stress versus engineering-strain curves are converted into their respective true stress versus true strain curves and parameterized.

3.1 Johnson-Cook Strength and Failure Models

While there is a relatively large selection of material models that can be used for parameterization of AA2139-T8 base-metal and weld-nugget materials, the Johnson-Cook deformation/strength and fracture model (Ref 15, 16) was used. This model is capable of representing the material behavior displayed under large-strain, high deformation rate, high-temperature conditions, of the type encountered in the problem of computational modeling of the ballistic/blast loading of a vehicle test-structure. Deformation/strength and failure components of this model are briefly reviewed below.

3.1.1 Deformation/Strength. Within this model, the subject material is considered as an isotropic linear-elastic and a strain-rate sensitive, strain-hardenable and (reversibly) thermally softenable plastic material. The deformation response of the material is defined using the following three relations: (a) a *yield criterion*, i.e., a mathematical relation which defines the condition which must be satisfied for the onset (and continuation) of plastic deformation; (b) a *flow rule*, i.e., a relation which describes the rate of change of different plastic-strain components during plastic deformation; and (c) a *constitutive*

law, i.e., a relation which describes how the material-strength changes as a function of the extent of plastic deformation, the rate of deformation and temperature. For most aluminum- and titanium-alloy grades used in military-vehicle FSWed structures, plasticity is considered to be of a purely distortional (non-volumetric) character and a von Misses yield criterion and a normality flow-rule are used. The von Misses yield criterion states that equivalent stress must be equal to the material yield strength for plastic deformation to occur/proceed. The normality flow-rule states that the plastic flow takes place in the direction of the stress-gradient of the yield surface (i.e., in a direction normal to the yield surface, when the latter is defined in the stress space). The Johnson-Cook strength constitutive law is defined as:

$$\sigma_y = \left[A + B(\bar{\varepsilon}^{\mathrm{pl}})^n\right]\left[1 + C\log(\dot{\bar{\varepsilon}}^{\mathrm{pl}}/\dot{\bar{\varepsilon}}_o^{\mathrm{pl}})\right]\left[1 - T_H^m\right] \qquad \text{(Eq 2)}$$

where $\bar{\varepsilon}^{\mathrm{pl}}$ is the equivalent plastic-strain, $\dot{\bar{\varepsilon}}^{\mathrm{pl}}$ the equivalent plastic-strain rate, $\dot{\bar{\varepsilon}}_o^{\mathrm{pl}}$ a reference equivalent plastic-strain rate, A the zero-plastic-strain, unit-plastic-strain-rate, room-temperature yield strength, B the strain-hardening constant, n the strain-hardening exponent, C the strain-rate constant, m the thermal-softening exponent and $T_H = (T - T_{\mathrm{room}})/(T_{\mathrm{melt}} - T_{\mathrm{room}})$ a room-temperature (T_{room})-based homologous temperature while T_{melt} is the melting temperature. All temperatures are given in Kelvin.

3.1.2 Failure. Within this model, the material failure is assumed to be of a ductile character and the progress of failure is defined by the following cumulative damage law:

$$D = \sum \frac{\Delta\varepsilon}{\varepsilon_f} \qquad \text{(Eq 3)}$$

where $\Delta\varepsilon$ is the increment in effective plastic-strain with an increment in loading, and ε_f is the failure strain at the current state of loading which is a function of the mean stress, the effective stress, the strain rate, and the homologous temperature, given by:

$$\varepsilon_f = D_1\left[1 + \frac{D_2}{D_1}\exp(-D_3\sigma^*)\right]\left[1 + D_4\ln\dot{\varepsilon}_{pl}\right]\left[1 + D_5 T_H\right] \qquad \text{(Eq 4)}$$

where σ^* is mean stress normalized by the effective stress. The parameters D_1, D_2, D_3, D_4, and D_5 are all material-specific constants. Failure is assumed to occur when D given in Eq 3 is equal to 1.0. It should be noted that, in contrast to, many "damage-type" materials constitutive models, a non-zero value of the damage variable D does not degrade the material's stiffness/strength but merely signals the moment of failure (when $D = 1.0$).

3.2 Model Parameterization

3.2.1 Base-Metal. Due to a relatively limited extent (i.e., a single strain-rate and room-temperature) of mechanical testing, not all the Johnson-Cook parameters could be determined from the experimental stress versus strain data. To overcome this shortcoming, the following procedure was implemented:

(a) a typical value m (=0.859, Ref 17) is assumed for the thermal softening part of the strength model;
(b) by comparing the present initial (quasi-static) yield strength with its dynamic counterpart reported in Ref 18, the strain-rate coefficient has been assessed as $C = 0.043$; and
(c) the remaining three strength parameters (A, B, n) are determined by a standard curve-fitting procedure to yield: $A = 307$ MPa, $B = 524$ MPa, and $n = 0.4$.

As far as the failure-model parameters are concerned, the last three parameters are assigned their typical values: $D_3 = 0.349$, $D_4 = 0.147$, and $D_5 = 16.8$ (Ref 19). To assess the remaining two failure parameters, D_1 and D_2, it is assumed that D_2/D_1 remains constant and equal to 28.5 (Ref 20). Then using Eq 4 and the experimentally determined value of the failure strain, the two unknown failure parameters are assessed as: $D_1 = 0.0125$ and $D_2 = 0.3554$.

3.2.2 Weld Nugget. The aforementioned procedure is next applied to the weld-nugget experimental stress versus strain data to yield: $A = 178$ MPa, $B = 524$ MPa, $n = 0.4$, $C = 0.043$, $m = 0.859$, $D_1 = 0.0268$, $D_2 = 0.7647$, $D_3 = 0.349$, $D_4 = 0.147$, and $D_5 = 16.8$. It should be noted that the same values for the strength parameters B and n were obtained as in the base-metal case. This was not fortuitous but rather the result of the fact that these two parameters were set equal in the two materials (Ref 20) and the material-model parameterization carried out for both materials simultaneously. Likewise, the failure parameters ratio D_2/D_1 was set equal in the two materials.

4. Two-Level Weld-Material-Homogenization Procedure

In this section, a new procedure is proposed and implemented for homogenization of the material within the individual FSW zones as well as within the entire weld.

4.1 First-Level Homogenization

As discussed earlier, only the base-metal and the weld-nugget quasi-static mechanical properties are determined experimentally in this study. On the other hand, a complete microhardness field plot is determined over the entire weld region. In this section, a simple procedure (based on the use of their experimentally measured microhardness values) is proposed for the assessment of the mechanical tensile properties of the remaining two weld zones, i.e., HAZ and TMAZ. The procedure is based on our recent study (Ref 9) which suggested that the initial yield strength (as represented by the Johnson-cook parameter A) scales with the material mean microhardness. This hypothesis is validated in this study, which shows that the ratio of the initial yield stress and the mean hardness for the base-metal (=307 MPa/130 kgf/mm^2 = 2.36) and the weld-nugget (=178 MPa/75 kgf/mm^2 = 2.37) are quite comparable.

Based on this finding, it is assumed that this ratio can be treated as a constant and set to an average value of 2.365. Then, using the mean microhardness values for the HAZ (=105 kgf/mm^2) and TMAZ (=120 kgf/mm^2), the corresponding Johnson-cook A-parameter values are determined as 248 and 283 MPa in the two zones, respectively. The remaining Johnson-cook strength parameters, B, n, C, and m are set equal to their counterparts in the base-metal/weld-nugget regions.

As far as the Johnson-Cook failure-model parameters are concerned, it is assumed, following the procedure established in

our recent study (Ref 9), that only parameter D_1 is affected by the FSW process (while the D_2/D_1 ratio is assumed constant, Ref 20). Using the D_1 values for the base-metal and weld-nugget and the corresponding mean hardness values, it is found that D_1 is proportional to the mean value of the microhardness, HV, raised to the power $-p$ (=−1.39). Using this relation and the respective microhardness values, D_1 is computed as 0.0168 and 0.0139 for the HAZ and TMAZ. Likewise, D_2 is computed from the constant ratio D_2/D_1 = 28.5 as 0.479 and 0.397 for the HAZ and TMAZ, respectively. Thus, the application of the first-level homogenization procedure described above yielded the previously unknown Johnson-Cook strength and failure-model parameters for the HAZ and TMAZ in AA2139.

To validate the procedure described above, a simple quasi-static finite-element analysis of the transverse-tensile test is conducted in which each weld zone is represented by a single homogenized material. The resulting stress-strain curve (labeled "Computational, Without Residual Stresses") is compared with its experimental counterpart (labeled "Experiment, Ref 10"), Fig. 7(a). It is seen that only a fair agreement is obtained between the computational and the experimental curves with respect to the initial-yielding portion of the curve, the overall hardening behavior and the final strain to failure. It should be noted that until now, no consideration was given to the presence of residual stresses within the different FSW weld-zones. While, this may be justified for the residual stresses aligned with the axial direction of the tensile sample, similar stress-relaxation effects cannot be assumed in the welding direction. To determine the effects of the latter residual stresses on the stress-strain behavior of the weldment in the transverse direction, the residual-stress results displayed in Fig. 6(b) are used to define the initial-stress condition in the aforementioned quasi-static finite-element analysis. The result of this analysis is also shown in Fig. 7(a) (the curve labeled "Computational, With Residual Stresses"). It is seen that substantial improvements in the experiment/computation agreement is obtained by accounting for the presence of residual stresses. The distribution of the Johnson-Cook damage variable, D, at the onset of fracture is displayed in Fig. 7(b). It is seen that failure occurs in the HAZ and this finding is fully consistent with the experimental observations (Ref 10). Based on the foregoing findings, it was concluded that the first-level homogenization procedure, within which each weld-zone is treated as a separate (homogenized) material and within which the effect of residual stresses is accounted for is physically sound.

4.2 The Second-Level Homogenization

In this section, homogenized weld-zone properties are combined into a single homogenized material representative of the entire weld.

To determine the initial strength of the resulting material, it is taken into account that the zones are fully joined and thus their mechanical response is fully kinematically coupled, i.e., the softer material will be restrained by the bordering harder-material and will yield at a higher stress-level than its yield stress. Based on this argument, it is assumed that the Johnson-Cook strength parameter A for the entire weld is a simple

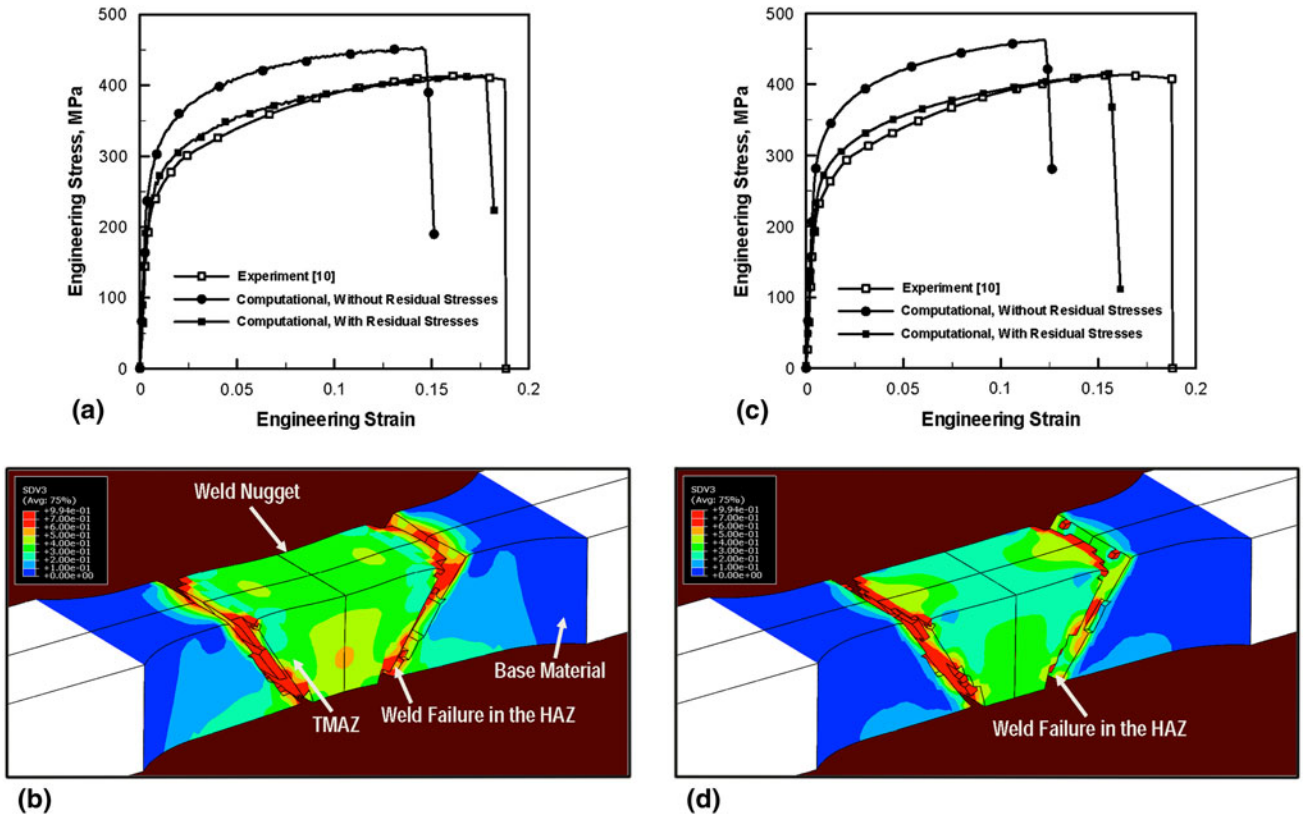

Fig. 7 (a) The predictions of the transverse stress/strain tensile curves and (b) the spatial distribution of the Johnson-Cook damage parameter at the onset of failure in the case of the first-level weld-material-homogenization procedure; (c, d) the corresponding results for the case of the second-level weld-material-homogenization procedure (please see text for details)

volume-based weighted average of the HAZ, TMAZ, and the weld-nugget A parameters, i.e.,

$$A_{\text{weld}} = f_{\text{HAZ}} \cdot A_{\text{HAZ}} + f_{\text{TMAZ}} \cdot A_{\text{TMAZ}} + f_{\text{nugget}} \cdot A_{\text{nugget}} \quad \text{(Eq 5)}$$

where, f represents the respective weld-zone volume fraction.

As far as ductility of the weld is concerned, it is assumed to be dominated by its least ductile zone and hence,

$$\frac{1}{D_{1,\text{weld}}} = \frac{f_{\text{HAZ}}}{D_{1,\text{HAZ}}} + \frac{f_{\text{TMAZ}}}{D_{1,\text{TMAZ}}} + \frac{f_{\text{nugget}}}{D_{1,\text{nugget}}} \quad \text{(Eq 6)}$$

Using the procedure described above, A_{weld} and $D_{1,\text{weld}}$ are determined as 215 MPa and 0.0152, respectively, while, $D_{2,\text{weld}} = 28.5 D_{1,\text{weld}}$. The remaining strength and failure weld parameters are set equal to their individual weld zone counterparts.

To validate the aforementioned homogenization procedure, the entire weld is modeled using a single homogenized material and the quasi-static finite-element analyses (without and with the considerations of residual stresses) of the transverse tensile test repeated. The results of the analyses are shown in Fig. 7(c). As in the case of Fig. 7(a), it is seen that the inclusion of the residual stresses improves the extent of experiment/computation agreement. In addition, as expected, this extent of agreement is somewhat compromised (but still acceptable) in the case of the second-level homogenization (Fig. 7a versus c). The results displayed in Fig. 7(d) show that the overall distribution of the Johnson-Cook damage parameter at the onset of failure and the fracture location are correctly predicted in the case of the second-level homogenization procedure. These finding are quite encouraging and suggests that the second-level homogenization procedure also yields physically sound results. Further validation and verification of the second-level homogenization procedure will be provided in the next section.

5. Validation and Verification

In this section, the foregoing two-level material-homogenization procedure is validated within the context of blast-survivability computational analyses of the military-vehicle test-structures.

5.1 Transient Non-Linear Dynamics Modeling of Blast-Survivability

5.1.1 General Considerations. First, a brief description is given of the computational analysis used to simulate the interactions between the detonation-products/soil-ejecta resulting from the explosion of a mine shallow-buried in soil under a military-vehicle test-structure. The computational modeling of these interactions involved two distinct steps: (a) geometrical and mesh modeling of the test-structure along with the accompanying mine and soil regions, and (b) the associated transient non-linear dynamics analysis of the impulse loading (momentum transfer) from the detonation-products/soil-ejecta to the test-structure and the kinematic and dynamic response of the structure.

All the calculations carried out in this portion of the study were done using ABAQUS/Explicit, a general purpose transient non-linear dynamics analysis software (Ref 21). In our previous study (Ref 9), a detailed account was provided of the basic features of ABAQUS/Explicit, emphasizing the ones which are most relevant for modeling detonation of shallow-buried and ground-laid mines and the subsequent interactions between detonation-products, soil-ejecta, and the test-structure. Therefore, only a brief overview of ABAQUS/Explicit is given in this section.

A typical transient non-linear dynamics problem such as the interactions between shallow-buried mine detonation-products and soil-ejecta with the test-structure is analyzed within ABAQUS/Explicit by solving simultaneously the governing partial differential equations for the conservation of mass, linear momentum, and energy along with the material constitutive equations and the equations defining the initial and the boundary conditions. The aforementioned equations are solved numerically using a second-order accurate explicit scheme. The ABAQUS/Explicit computational engine solves the governing equations within a Lagrange framework, i.e., the computational finite-element grid is tied to the attendant components/materials (soil, the mine, and the test-structure, in the present case) and moves and deforms with them.

Interactions between the various components of the model (mine detonation-products, soil, and the test-structure, in the present case) are typically accounted for using the "Hard Contact Pair" type of contact algorithm. Within this algorithm, contact pressures between two bodies are not transmitted unless the nodes on the "slave surface" contact the "master surface." No penetration/over closure is allowed and there is no limit to the magnitude of the contact pressure that could be transmitted when the surfaces are in contact. Transmission of shear stresses across the contact interfaces is defined in terms of a static and a kinematic friction coefficient and an upper-bound shear stress limit (a maximum value of shear stress which can be transmitted before the contacting surfaces begin to slide).

In a typical blast-survivability test-structure computational analysis, the following steps are taken: (a) at the beginning of the simulation, the test-structure, the mine and the soil are all assumed to be at rest (with the gravitational force acting downward); (b) mine detonation is next initiated either over the entire bottom face of the mine or at the bottom center; and (c) the mechanical response of the test-structure to impact by the soil-ejecta and the detonation-products is monitored to quantify the test-structure blast-survivability. To ensure fidelity of this approach, i.e., to ensure that the results obtained are insensitive to the size of the elements used, a standard mesh-sensitivity analysis needs to be carried out (the results not shown for brevity).

5.1.2 Geometrical and Meshed Models. *Military-Vehicle Test-Structure.* A geometrical model of the military-vehicle test-structure analyzed in this study is depicted in Fig. 8. The CAD model shown in this figure was created in accordance with the test-structure description provided in Ref 22. It is seen that the test-structure represents the forward one-third portion of a typical Advanced Amphibious Assault Vehicle (AAAV) which is designed to withstand severe ballistic/blast threats. The test-structure assembly (with an overall length of ca. 2.6 m and width of 1.7 m) consists of the following AA2139-T8 FSWed components: (a) 25.4 mm thick floor plate; (b) 25.4 mm thick lower glacis (representing the lower forward portion of the test-structure); (c) 50.8 mm thick sidewalls; (d) chine actuator mounts fabricated from 25.4 and 50.8 mm thick plates; and (e) 25.4 mm thick transition piece connecting the lower glacis and the floor plate.

The CAD model was next preprocessed (meshed) using the general purpose pre-processing program HyperMesh from

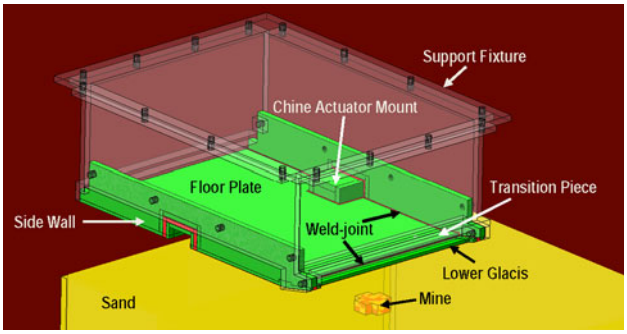

Fig. 8 An example of the (sub-scale) vehicle-underbody structure

Altair Inc. (Ref 23). The resulting meshed model of the test-structure consists of approximately 700,000 and 9,000,000 six- and eight-node prismatic and 4-node tetrahedron first-order reduced-integration continuum elements when the weld-zone is represented as a single zone and multiple-zones, respectively.

Mine and Soil Regions. The mine and soil computational domains used in this study are shown in Fig. 8. The size and circular-disk shape of the mine computational domain are selected to match that of a typical 7 kg anti-vehicle C4 mine used in Ref 27. The mine computational domain was meshed using eight-node first-order reduced-integration continuum elements with a typical edge-length of 5 mm and filled with a C4 HE material.

The soil computational domain was modeled as a solid cuboid with $L \times W \times H = 3400 \times 3400 \times 1500$ mm. The domain was divided into three concentric sub-domains. All three sub-domains were meshed using eight-node reduced-integration continuum elements with a typical edge-length of 5 mm in the inner-most sub-domain and a typical edge-length of 50 mm in the outer-most sub-domain. The lateral and the bottom faces of the soil domain were subsequently surrounded with eight-node infinite elements to model far-field soil regions and avoid un-physical stress-wave reflection at the soil-domain lateral and bottom surfaces. The soil domains containing non-infinite elements were filled with CU-ARL soil material (discussed later), while the infinite elements were filled with an "elastic" soil material with a Young's modulus and a Poisson's ratio matching those of the CU-ARL soil.

5.1.3 Material Models. As discussed above, the complete definition of a transient non-linear dynamics problem entails the knowledge of the material models that define the relationships between the flow variables (pressure, mass-density, energy-density, temperature, etc.). These relations typically involve: (a) an equation of state; (b) a strength equation; (c) a failure equation, and (d) an erosion equation for each constituent material. These equations arise from the fact that, in general, the total stress tensor can be decomposed into a sum of a hydrostatic stress (pressure) tensor (which causes a change in the volume/density of the material) and a deviatoric stress tensor (which is responsible for the shape change of the material). An equation of state then is used to define the corresponding functional relationship between pressure, mass-density, and internal energy density (temperature). Likewise, a (constitutive material) strength relation is used to define the appropriate equivalent plastic-strain, equivalent plastic-strain rate, and temperature dependencies of the materials yield strength. This relation, in conjunction with the appropriate yield-criterion and flow-rule relations, is used to compute the deviatoric part of stress under elastic-plastic loading conditions. In addition, a material model generally includes a failure criterion (i.e., an equation describing the hydrostatic or deviatoric stress and/or strain condition(s)) which, when attained, cause the material to fracture and lose its ability to support (abruptly in the case of brittle materials or gradually in the case of ductile materials) normal and shear stresses. Such failure criterion in combination with the corresponding material-property degradation and the flow-rule relations governs the evolution of stress during failure. The erosion equation is generally intended for eliminating numerical solution difficulties arising from highly distorted elements. Nevertheless, the erosion equation is often used to provide additional material failure mechanism especially in materials with limited ductility.

To summarize the above, the equation of state along with the strength and failure equations (as well as with the equations governing the onset of plastic deformation and failure and the plasticity and failure induced material flow) enables assessment of the evolution of the complete stress tensor during a transient non-linear dynamics analysis. Such an assessment is needed where the governing (mass, momentum, and energy) conservation equations are being solved. Separate evaluations of the pressure and the deviatoric stress enable inclusion of the nonlinear shock-effects in the equation of state.

In this study, the following materials are utilized within the computational domain: C4 HE explosive, AA 2139-T8 (base-metal, various weld-zones, and the weld as a whole), and soil. Since a detailed account of the constitutive models used to represent the behavior of the materials in question can be found in our recent study (Ref 9), only a brief qualitative description of these models will be provided in the remainder of this section.

C4 HE Explosive. The Jones-Wilkins-Lee (JWL) equation of state (Ref 24) is used for C4 in this study since that is the preferred choice for the equation of state for high-energy explosives in most hydrodynamic calculations involving detonation. Within a typical hydrodynamic analysis, detonation is modeled as an instantaneous process which converts un-reacted explosive into gaseous detonation-products and detonation of the entire high-explosive material is typically completed at the very beginning of a given simulation. Consequently, no strength and failure models are required for high-energy explosives such as C4.

AA 2139-T8. Since hydrostatic stress gives rise to only minor reversible density changes in metallic materials like AA 2139-T8, a linear type of equation of state was used for AA2138-T8. As discussed earlier, to represent the constitutive response of AA 2139-T8 (base-metal and weld) under deviatoric stress, the Johnson-Cook strength model (Ref 14) is used. Since AA2139-T8 base-metal and weld both exhibit a ductile mode of failure, their failure condition was defined using the Johnson-Cook failure model (Ref 15). Erosion of AA2139-T8 components is assumed to take place when the Johnson-Cook damage state-variable D, as defined by Eq 3, reaches a value of 1.0. When a material element is eroded, its nodes are retained along with their masses and velocities to conserve momentum of the system. The momentum is conserved by distributing the mass and velocities associated with the eroded elements among the

corner nodes of the remaining elements. Despite the fact that some loss of accuracy is encountered in this procedure (due to removal of the strain energy from the eroded elements), the procedure is generally found to yield reasonably accurate results (Ref 14).

Soil. Soil is a very complicated material whose properties vary greatly with the presence/absence and relative amounts of various constituent materials (soil particles, clay, silt, gravel, etc.), and particle sizes and particle size distribution of the materials. In addition, the moisture content and the extent of pre-compaction can profoundly affect the soil properties. To account for all these effects, Clemson University and the Army Research Laboratory (ARL), Aberdeen, Proving Ground, MD jointly developed (Ref 25-27) and subsequently parameterized (using the results of a detailed investigation of dynamic response of soil at different saturation levels, as carried out by researchers at the Cavendish Laboratory, Cambridge, UK; Ref 28) the CU-ARL soil model. This model (used in this study) is capable of capturing the effect of moisture on the dynamic behavior of soil and was named the CU-ARL soil model.

For the CU-ARL soil model, a saturation-dependant porous-material/compaction equation of state is used which, as shown in our previous study (Ref 25) is a particular form of the Mie-Gruneisen equation of state (Ref 29). Within this equation, separate pressure versus density relations are defined for plastic compaction (gives rise to the densification of soil) and for unloading/elastic-reloading. Within the CU-ARL soil strength model, the yield strength is assumed to be pressure-dependant and to be controlled by saturation-dependant inter-particle friction. In addition to specifying the yield stress versus pressure relationship, the strength model entails the knowledge of the density and saturation-dependent shear modulus. Within the CU-ARL soil failure model, failure is assumed to occur when the negative pressure falls below a critical saturation-dependant value, i.e., a "hydro"-type failure mechanism was adopted. After failure, the failed material element loses the ability to support tensile or shear loads while its ability to support compressive loads is retained. Erosion of a soil element is assumed, within the CU-ARL soil erosion model, to take place when geometrical (i.e., elastic plus plastic plus damage) instantaneous strain reaches a maximum allowable value. The investigation reported in Ref 26 established that the optimal value for the geometrical instantaneous strain is ~1.0.

5.2 Results and Discussion

The foregoing computational analysis of mine-blast and of subsequent interactions between detonation-products/soil-ejecta and the target structure was conducted in such a way that it would reveal the intrinsic blast-survivability of the structure. While the geometrical models used are somewhat simplified, they still retain the essential structural details of a vehicle underbody. Typically, blast-survivability of a vehicle test-structure is judged by a lack of penetration of the structure by the soil-ejecta and gaseous detonation-products and by the absence of excessive deflection. In addition, in the case when the test-structure has survived mine-blast impact, the extent of its damage is quantified to estimate the potential loss of vehicle mobility and the extent of repair needed to make the structure suitable for future use.

Examples of the typical (qualitative) results pertaining to the floor-plate total displacements and the associated extents of weld failure obtained in this portion of the study are depicted in Fig. 9(a), (b). Figure 9(a) displays the results obtained using a computationally more expensive analysis, in which the different weld-zones are represented explicitly. For comparison, Fig. 9(b) displays the corresponding results obtained in a computational analysis in which the weld-zones were homogenized into a single weld domain. Due to the sensitive nature of the subject matter and the potential for misuse of the quantitative results, quantitative details pertaining to the results displayed in Fig. 9(a), (b) could not be presented here. What could be said is that under a relatively large range of mine-blast loading conditions (associated with different mine shape and size, depth of burial, stand of distance, and mine placement relative to the test-structure), a fairly good agreement was obtained between the results of more detailed and the more efficient computational analyses. Typically, the penetration/no-penetration condition was correctly predicted, maximum deflection differed by less than 7%, the location of the welded structure cracking was correct and the crack propagation direction was consistent. What was not always correctly predicted by the computationally more efficient analysis was the extent of crack propagation (generally over-predicted) and the overall degree of weld cracking (generally over-predicted).

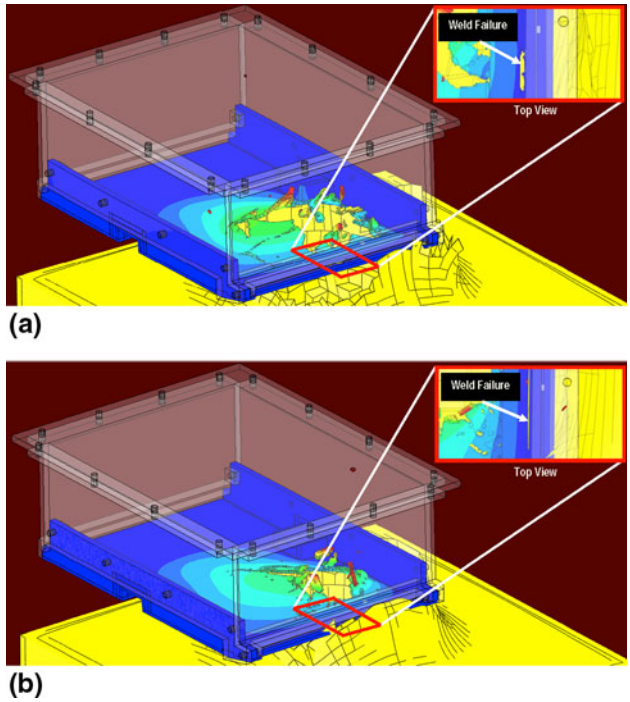

Fig. 9 A comparison of the results obtained using (a) a computational analysis with explicit weld-zone representation and (b) a computational analysis with homogenized weld-domains (please see text for details)

6. Summary

Based on the study presented and discussed in this article, the following main summary remarks and conclusions can be made:

1. A two-step weld-material-homogenization procedure is introduced to reduce the computational cost associated

with transient non-linear dynamics analyses of military-vehicle test-structure blast-survivability.
2. To demonstrate the utility of this procedure, microstructure, mechanical properties, and residual stresses are characterized for the case of AA2139-T8 friction-stir weldments.
3. Homogenization of different weld-zone materials (and the weld as a whole) is carried out within the context of Johnson-Cook deformation/strength and failure material models for the vehicle test-structure.
4. The procedure is validated by comparing the associated blast-survivability vehicle test-structure computational results with their computational counterparts obtained in a substantially more costly analysis in which welds are represented in more details.

References

1. M. Grujicic, G. Arakere, H.V. Yalavarthy, T. He, C.-F. Yen, and B.A. Cheeseman, Modeling of AA5083 Material-Microstructure Evolution During Butt Friction-stir Welding, *J. Mater. Eng. Perform.*, 2010, **19**(5), p 672–684
2. M. Grujicic, G. Arakere, C-F. Yen, and B.A. Cheeseman, Computational Investigation of Hardness Evolution during Friction-stir Welding of AA5083 and AA2139 Aluminum Alloys, *J. Mater. Eng. Perform.*, 2010, doi:10.1007/s11665-010-9741-y
3. M. Grujicic, G. Arakere, B. Pandurangan, A. Hariharan, C-F. Yen, B.A. Cheeseman, and C. Fountzoulas, Statistical Analysis of High-Cycle Fatigue Behavior of Friction Stir Welded AA5083–H321, *J. Mater. Eng. Perform*, doi:10.1007/s11665-010-9725-y, July 2010
4. M. Grujicic, T. He, G. Arakere, H.V. Yalavarthy, C.-F. Yen, and B.A. Cheeseman, Fully-Coupled Thermo-Mechanical Finite-element Investigation of Material Evolution During Friction-Stir Welding of AA5083, *J. Eng. Manuf.*, 2010, **224**(4), p 609–625
5. W.M. Thomas, E.D. Nicholas, J.C. Needham, M.G. Murch, P. Temple-Smith, and C.J. Dawes. Friction Stir Butt Welding, International Patent Application No. PCT/GB92/02203 (1991)
6. M. Grujicic, G. Arakere, B. Pandurangan, A. Hariharan, C-F. Yen, and B.A. Cheeseman, Development of a Robust and Cost-effective Friction Stir Welding Process for use in Advanced Military Vehicle Structures, *J. Mater. Eng. Perform.*, 2010, doi:10.1007/s11665-010-9650-0
7. M. Grujicic, G. Arakere, B. Pandurangan, A. Hariharan, C-F. Yen, B.A. Cheeseman, and C. Fountzoulas, Computational Analysis and Experimental Validation of the Ti-6Al-4V Friction Stir Welding Behavior, *J. Eng. Manuf.* (pending approval from sponsor for manuscript submission), January 2010
8. W. Van Haver, B. de Meester, A. Geurten, and J. Defrancq, Innovative Joining of Critical Aluminium Structures with the Friction Stir Welding Technique—CASSTIR, Final Report, Belgian Science Policy (Programme to stimulate knowledge transfer in areas of strategic importance—TAP2), Brussels, 2010, 110
9. M. Grujicic, G. Arakere, A. Hariharan, B. Pandurangan, C-.F. Yen, and B.A. Cheeseman, A Concurrent Design, Manufacturing and Testing Product Development Approach for Friction-stir Welded Vehicle Underbody Structures, *J. Manuf. Eng. Perform.* August, 2010 (submitted)
10. W. Mohr, APP09 Task 2.5 Mechanical Properties of FSW 2XXX and 5XXX Alloys, EWI Project No. 51972GTH, Edison Welding Institute, 2009
11. J.W.L. Pang, T.M. Holden, and T.E. Mason, In-situ Generation of Intergranular Strains in an Al7050 Alloy, *Acta Mater.*, 1998, **46**(5), p 1503–1518
12. M.R. Daymond, C.N. Tome, and M.A.M. Bourke, Measured and Predicted Intergranular Strains in Textured Austenitic Steel, *Acta Mater.*, 2000, **48**, p 553–564
13. I.C. Noyan and J.B. Cohen, *Residual Stress: Measurement by Diffraction and Interpretation*, Springer-Verlag, New York, 1987
14. M. Peel, A. Steuwer, M. Preuss, and P.J. Withers, Microstructure, Mechanical Properties and Residual Stresses as a Function of Welding Speed in Aluminium AA5083 Friction-Stir Welds, *Acta Mater.*, 2003, **51**, p 4791–4801
15. G.R. Johnson and W.H. Cook, A Constitutive Model and Data for Metals Subjected to Large Strains, High Strain Rates and High Temperatures, *Proceedings of the 7th International Symposium on Ballistics*, 1983
16. G.R. Johnson and W.H. Cook, Fracture Characteristics of Three Metals Subjected to Various Strains, Strain Rates and Temperatures, *Eng. Fract. Mech.*, 1985, **21**(1), p 31–48
17. *Autodyn Materials Library*, Ansys/Autodyn 11.0, Ansys Inc. 2010
18. Southwest Research Institute, work in progress, 2010
19. A.H. Clausen, T. Borvik, O.S. Hopperstad, and A. Benallal, Flow and Fracture Characteristics of Aluminum Alloy AA5083–H116 as Function of Strain-rate, Temperature and Triaxiality, *Mater. Sci. Eng. A*, 2004, **364**, p 260–272
20. C-F. Yen, ARL, Aberdeen Proving Ground, MD, work in progress, October 2010
21. *ABAQUS 6.9*, Theory Manual, Dassault Systemes, 2010
22. K.J. Colligan, P.J. Konkol, J.J. Fisher, and J.R. Pickens, Friction Stir Welding Demonstrated for Combat Vehicle Construction, *Weld. J.*, 2003, **82**(3), p 34–40
23. *HyperMesh 10.0*, Theory Manual, Altair Engineering Inc., 2010
24. E.L. Lee, H.C. Hornig, and J.W. Kury, *Adiabatic Expansion of High Explosive Detonation Products, UCRL–50422*, Lawrence Radiation Laboratory, University of California, California, 1968
25. M. Grujicic, B. Pandurangan, and B.A. Cheeseman, The Effect of Degree of Saturation of Sand on Detonation Phenomena Associated with Shallow-buried and Ground-laid mines, *Shock Vib.*, 2006, **13**, p 41–62
26. M. Grujicic, B. Pandurangan, Y. Huang, B.A. Cheeseman, W.N. Roy, and R.R. Skaggs, Impulse Loading Resulting from Shallow Buried Explosives in Water-saturated Sand, *J. Mater. Des. Appl.*, 2007, **221**, p 21–35
27. M. Grujicic, B. Pandurangan, R. Qiao, B.A. Cheeseman, R.R. Skaggs, and R. Gupta, Parameterization of the Porous-Material Model for Sand with Different Levels of Water Saturation, *Soil Dyn. Earthq. Eng.*, 2008, **28**, p 20–35
28. A.M. Bragov, A.K. Lomunov, I.V. Sergeichev, K. Tsembelis, and W.G. Proud, Determination of Physicomechanical Properties of Soft Soils from Medium to High Strain Rates, *Int. J. Impact Eng.*, 2008, **35**(9), p 967–976
29. ANSYS/Autodyn-2D and 3D, Version 11, *User Documentation*, Ansys Inc., 2007